Materials Today Bio 16 (2022) 100452

Contents lists available at ScienceDirect

Materials Today Bio

journal homepage: www.journals.elsevier.com/materials-today-bio

Engineering Fe/Mn-doped zinc oxide nanosonosensitizers for ultrasound-activated and multiple ferroptosis-augmented nanodynamic tumor suppression

Zhongqian Hu [a], Xinran Song [d], Li Ding [d], Yu Cai [a], Luodan Yu [b,****], Lijuan Zhang [c,***], Yajun Zhou [c,**], Yu Chen [b,*]

[a] Department of Ultrasound and Radiology, Zhongda Hospital, Medical School, Southeast University, Nanjing, 210009, PR China
[b] Materdicine Lab, School of Life Sciences, Shanghai University, Shanghai, 200444, PR China
[c] Department of Ultrasound, The Fourth Affiliated Hospital, Nanjing Medical University, Nanjing, 210029, PR China
[d] Department of Medical Ultrasound, Shanghai Tenth People's Hospital, Ultrasound Research and Education Institute, Tongji University Cancer Center, Shanghai Engineering Research Center of Ultrasound Diagnosis and Treatment, Tongji University School of Medicine, Shanghai, PR China

ARTICLE INFO

Keywords:
Sonodynamic therapy
Reactive oxygen species
Nanoparticles
Ferroptosis
Glutathione

ABSTRACT

As an effective tumor-therapeutic modality, ultrasound-triggered sonodynamic therapy (SDT) has been extensively explored to induce cancer cell death by activating sonosensitizers to generate reactive oxygen species (ROS). However, the traditional inorganic semiconductor-based sonosensitizers still suffer from inefficient ROS production because of the low separation efficiency of electrons and holes (e^-/h^+) and their fast recombination. Herein, the iron (Fe) and manganese (Mn) co-doped zinc oxide nanosonosensitizers have been rationally designed and engineered for augmenting the SDT efficiency against tumor by inducing both multiple ferroptosis and apoptosis of tumor cells. The Fe/Mn component was co-doped into the nannostructure of ZnO nanosonosensitizers, which not only catalyzed the Fenton reaction in the hydrogen peroxide-overexpressed tumor microenvironment to produce ROS, but also depleted intracellular glutathione to suppress the consumption of ROS. The doping nanostructure in the engineered nanosonosensitizers substantially augmented the SDT efficacy of ZnO nanosonosensitizers by promoting the separation and hindering the recombination of e^-/h^+ under ultrasound activation. The multiple ferroptosis and apoptosis in the enhanced SDT effect of Fe/Mn co-doped ZnO nanosonosensitizers were solidly demonstrated both *in vitro* and *in vivo* on tumor-bearing mice in accompany with the detailed mechanism assessment by RNA sequenching. This work provides a distinct strategy to augment the nanomedicine-enabled SDT efficency by engineering the inorganic semiconductor-based nanosonosensitizers with transitional metal doping and inducing multiple cell-death pathways including ferroptosis.

1. Introduction

Malignancy has threatened the human health for centuries with its high mortality [1–3]. Remarkble advances in the field of nanotherapy have provided tremendous opportunities for human to fight against tumor [4–14]. Among all possible efforts made by reserachers, sonodynamic therapy (SDT) presents a promising cancer treatment modality because of its noninvasiveness and deep tissue penetration [15–19]. SDT employs ultrasound (US) to activate sonosensitizers for generating toxic reactive oxygen species (ROS), which further evokes apoptosis of tumor cells. For inorganic semiconducotor-based SDT, when US irradiates on sonosensitizers, the electrons (e^-) transfer from the valence band (VB) to the conduction band (CB), and the holes (h^+) will form in the VB. Then, the highly active e^- and h^+ can further react with oxygen (O_2) and water molecules (H_2O) to generate different kinds of ROS. As the US features deep tissue penetration and high controllability, SDT is of great protential for tumor nanotherapy as compared to traditional photodynamic therapy, especially for tumor in deep site of body [20–23].

* Corresponding author.
** Corresponding author.
*** Corresponding author.
**** Corresponding author.
E-mail addresses: yuluodan@shu.edu.cn (L. Yu), zlj1975726@126.com (L. Zhang), zhouyajun900804@163.com (Y. Zhou), chenyuedu@shu.edu.cn (Y. Chen).

https://doi.org/10.1016/j.mtbio.2022.100452
Received 25 August 2022; Received in revised form 1 October 2022; Accepted 4 October 2022
Available online 5 October 2022

However, SDT-based tumor treatment is still at the preliminary stage of development and has not been extensively applied in clinic because of the unsatisfactory anti-tumor efficacy and unclear biological effects. Since the success of SDT highly denpends on the performance of sonosensitizers, both organic and inorganic sonosensitizers have been explored and utilized recently [24–26]. Organic sonosensitizers, including porphyrins and porphyrin derivatives, typically suffer from the critical issues of poor stability, fast clearance and high phototoxicity, resulting in unsatisfactory efficacy against tumor and potential biotoxicity *in vivo* [27]. In contrast, inorganic semiconductor-based sonosensitizers, such as zinc oxide (ZnO) nanoparticles, are more preferable for effective SDT-based tumor treatment with high stability and low phototoxicity [28–32]. As a typical semiconductor, the electrons in ZnO are transferred from VB to CB opon US irradiation, resulting in the separation of e^- and h^+, which further react with O_2 and H_2O to produce $^1O_2$ and •OH [33,34]. However, due to the rapid recombination rate of e^- and h^+, the therapeutic limitation of ZnO sonosensitizers still exists, which would reduce the production of ROS. Therefore, it is highly necessary to explore more effective inorganic semiconductor-based sonosensitizers to reduce the recombination of e^- and h^+ in SDT under ultrasonic activation.

Inspired by the optical and electronic properties of ZnO, which has great potential in nanoelectronic applications, doping of metal component in ZnO is an effective method to improve the semiconducting properties [35–37]. The doping transition metals typically include iron (Fe) and manganese (Mn) elements. After doping into ZnO, Fe^{3+} and Mn^{4+} could attrack e^- so as to form oxygen vacancy in ZnO, which leads to the decrease of e^-/h^+ recombination. Moreover, Fe^{2+} and Mn^{2+} can react with tumor-overexpressed H_2O_2 in tumor site for triggering the typical Fenton reaction, which generates the highly toxic •OH for inducing the enhanced SDT effect [29,38–41].

Herein, the Fe/Mn-doping ZnO nanoparticle (D-ZnO NP) was designed and constructed by adding Fe and Mn source to the Zn precursor solution during the synthetic procedure. The as-synthesized D-ZnO NP could not only induce the ferroptosis effect in the presence of Fe and Mn, but also augment SDT effect by decreasing the recombination of e^-/h^+ pairs. In detail, the Fe^{3+} and Mn^{4+} doping could oxidize glutathione (GSH) to glutathione disulfide (GSSH), which decreases the consumption of ROS. In addition, during the GSH depletion process, the Fe^{3+} and Mn^{4+} were respectively reduced to Fe^{2+} and Mn^{2+}, which could trigger Fenton-like cataytic reaction in the presence of tumor-overexpressed H_2O_2 in the tumor microenvironment (TME). Thus, the ferroptosis effect was induced. Furthermore, the D-ZnO also performed better SDT effect than pure ZnO. On one hand, the doping of Fe and Mn could effectively separate the e^-/h^+ pairs by reducing the band gap. On the other hand, the Fe^{3+} and Mn^{4+} could decrease the recombination of e^-/h^+ pairs by attracting e^-. After polyethylene glycol (PEG) surface modification, the D-ZnO-PEG NPs could accumulate in the tumor site by enhanced permeation retention (EPR) effect after intravenous administration and subsequently achieve the ferroptosis-augmented SDT on suppressing tumors under US irradiation. Therefore, our work successfully designed and fabricated a high-performance nanosonosensitizer based on trasitional metal doping to achieve highly efficient tumor-therapeutic outcome (Fig. 1).

2. Results and discussion

2.1. Fabrication and characterization of D-ZnO-PEG NPs

The D-ZnO NPs were synthesized by a simple nonaqueous sol-gel method [35]. Briefly, the pure ZnO NPs were prepared by adding 1.89 mmol Zn acetylacetonate hydrate to 10 ml anhydrous benzyl alcohol, then the mixture was heated in a Teflon autoclave at 200 °C for 3 days. The white ZnO nanorods (NRs) were obtained after washing several times by ethanol. During the synthesis procedure, 10 mol% of Fe acetylacetonate and 10 mol% of Mn acetylacetonate were added to the reaction mixture, by which the doping was achieved (Fig. 2a). Transmission electron microscopy (TEM) image showed that the pure ZnO NRs featured the average size of 70 nm (Fig. 2b). The as synthesized D-ZnO presented globular morphology compared with the rod-like pure ZnO according to TEM image (Fig. 2c). The high-angle annular dark-field scanning TEM (HAADF-STEM) images exhibited that the engineered D-ZnO NPs remained uniform and discrete with the average size of ~70 nm (Fig. 2d and e).

To confirm the success of Fe/Mn doping, the elemental mapping, energy dispersion spectrum (EDS) and the high-resolution TEM (HRTEM) were applied. For the elemental mapping and EDS, the distribution of O, Zn, Fe and Mn was present in D-ZnO NPs (Fig. 2f, S1). The HRTEM images provided a closer observation of the crystal structure in D-ZnO, and the lattice space was measured to be 0.26 nm (Fig. 2g and h). To discuss the element-valance status of Fe and Mn in D-ZnO NPs, X-ray photoelectron spectroscopy (XPS) was applied (Fig. S2). The Mn^{2+}/Mn^{4+} and Fe^{2+}/Fe^{3+} all existed in the structure of D-ZnO NPs (Fig. 2i and j).

In order to improve the biocompatibility and stability of D-ZnO NPs in physiological solution and enable their further biomedical application, mPEG-NH_2 was employed for surface modification. To confirm the successful PEGylation of D-ZnO-PEG, Fourier transform infrared (FT-IR) was applied to analyze the linkage of mPEG-NH_2. The absorption bands at 1210 cm^{-1} and 1156 cm^{-1} were ascribed to C–O stretching vibration of PEG, which demonstrated the successful PEGylation (Fig. S3) [42,43]. After PEGylation, the morphology of D-ZnO-PEG showed barely variation, which indicated the stability of the nanoparticle structure (Fig. S4). Afterwards, the diameters of D-ZnO-PEG NPs in different solutions were measured by dynamic light scattering (DLS). The results displayed around 95 nm in water, 138 nm in phosphate buffered saline (PBS) and 146 nm in fetal bovine serum (FBS), respectively (Fig. S5), which indicated the high dispersity of the as-prepared D-ZnO-PEG NPs for guaranteeing both *in vitro* and *in vivo* applications.

2.2. In vitro ferroptosis-augmented SDT performance

To assess the SDT performance of D-ZnO-PEG NPs, we employed 1,3-diphenylisobenzofuran (DPBF) as the probe of $^1O_2$ to monitor the ROS production. DPBF was added into different groups of solutions (Control, US, D-ZnO-PEG and D-ZnO-PEG + US). Each group was added with 0.1 mM H_2O_2, and the absorbance intensity of DPBF at 410 nm was recorded and analyzed by UV–vis spectrometer. The DPBF in D-ZnO-PEG + US group exhibited more decrease rate of intensity than that in the Control, US, ZnO-PEG + US group, indicating better SDT effect of D-ZnO than pure ZnO by generating $^1O_2$ (Fig. 3a and b). Moreover, different groups of solutions based on doping content (0%, 3%, 5% and 10% D-ZnO-PEG NPs) were also analyzed. The DPBF in 10% D-ZnO-PEG + US group exhibited more decrease rate than that in other groups (0%, 3% and 5%), indicating the distinct effect of enhanced SDT by promoting e^-/h^+ sepration and hindering their recombination (Fig. S6). Electron spin resonance (ESR) was employed to further detect the $^1O_2$ generation quantitatively. Compared with the Control, US, and ZnO-PEG + US group, the D-ZnO-PEG + US group exhibited the highest singlet oxygen intensities, which further confirmed the enhanced SDT effect of D-ZnO-PEG NPs (Fig. 3c).

Furthermore, we employed 3,3,5,5-tetramethylbenzidine (TMB) as the probe of •OH. Briefly, TMB and 0.1 mM H_2O_2 were mixed with different groups of solution (Control, US, D-ZnO-PEG, D-ZnO-PEG + US), and the characteristic peak at 650 nm was recorded afterwards. Noteworthly, the D-ZnO-PEG group showed nonnegligible increase of intensity, indicating the Fenton reaction of the doped Fe/Mn in ZnO NPs. Furthermore, when US was applied, the characteristic peak of D-ZnO-PEG + US group inceased most significantly, confirming the enhanced SDT effect of D-ZnO-PEG triggered by US irradiation (Fig. 3d and e). ESR was also employed to quantitatively detect the •OH production. As predicted, the D-ZnO-PEG + US group exhibited the highest increase of intensity, corresponding to the results of TMB •OH detection (Fig. 3f).

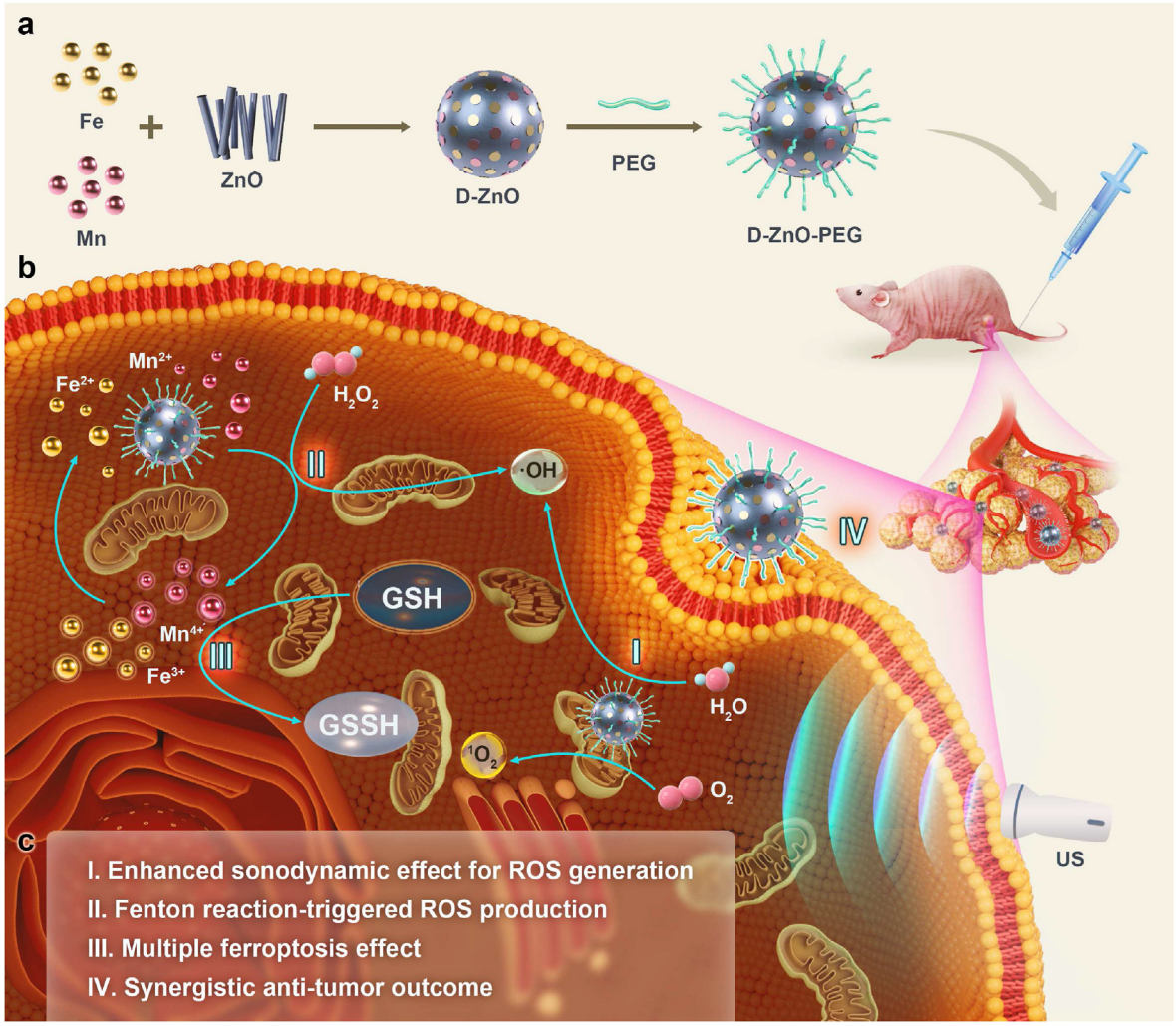

Fig. 1. Schematic illustration of the synthesis of D-ZnO-PEG nanosonosensitizers and the ferroptosis-augmented SDT anti-tumor effect. (a) The fabrication of D-ZnO NPs and further surface PEGylation. (b) The *in vivo* ferroptosis-augmented SDT effect after intravenous administration into 4T1 tumor-bearing mice, including catalytic Fenton reaction, GSH consumption and enhanced ROS production by SDT effect. (c) Main process in the ferroptosis-augmented SDT procedure by the D-ZnO-PEG nanosonosensitizers.

To investigate the underlying mechanism of the ferroptosis-augmented SDT effect, we first took GSH into consideration. As reducing substances, GSH can react with intracellular oxidizing agents and provent them from damaging cell membrane and mitochondrion, which could protect tumor cells from being killed by ROS [44]. Therefore, it is important to consume GSH during the procedure of ferroptosis-augmented SDT. To confirm the GSH consumption capability of D-ZnO-PEG NPs, we used UV–vis spectrometer to detect the GSH depletion. As shown in Fig. 3g, the GSH consumption was enhanced obviously as the concentration of D-ZnO-PEG increased. The D-ZnO-PEG + US group exhibited more GSH consumption than ZnO-PEG + US group because of the existense of Fe/Mn in these doping NPs. Notebly, the D-ZnO-PEG + US group also induced greater degree of GSH depletion than D-ZnO-PEG group. When US was applied, GSH was further oxidized by US-triggered ROS during the SDT procedure (Fig. 3h). Furthermore, the underlying mechanism of enhanced SDT effect by such doping nanostructure was also studied. It has been demonstarted that ZnO is a semiconductor with the band gap of about 3.37 eV, from VB to CB [45]. Herein, we plotted the Tauc plot of the Kubelka-Munk function to calculate the band gap of D-ZnO after the solid ultraviolet spectrum was recorded [46]. The band gap was determinded to be 2.02 eV, which was significantly lower than that of pure ZnO (3.37 eV), indicating the capability of easier triggering of e^- stimulation from VB to CB by US irradiation (Fig. 3i). Moreover, the Fe^{3+} and Mn^{4+} in such doping structure could attract the activated e^-, so as to hinder e^-/h^+ from recombination. In this way, ROS production was improved and SDT effect was enhanced.

2.3. Intracellular ferroptosis-augmented SDT performance

The *in vitro* anti-tumor effect of D-ZnO-PEG NPs was further evaluated on 4T1 cancer cell (a mouse breast cancer cell model). First of all, the effective cellular uptake is a vital ensurance for therapeutic effects. Therefore, we employed confocal laser scanning microscopy (CLSM) to observe the cellular uptake of D-ZnO-PEG NPs by 4T1 cells after labeling D-ZnO-PEG with fluorescein isothiocyanate (FITC) and 4T1 cells with 4′,6-diamidino-2-phenylindole (DAPI). After co-incubating 4T1 cells with D-ZnO-PEG NPs, the intensity of green fluorescence increased with time lasting and matched well with blue fluorescence of nucleus at 8 h, which indicated large amount of cellular uptake of D-ZnO-PEG NPs by endocytosis (Fig. S7). The typical cell-counting kit 8 (CCK-8) assay was further applied to evaluate the intracellular anti-tumor effect of D-ZnO-PEG NPs. The cell viability was calculated after different groups of treatments. The cytotoxicity of D-ZnO-PEG NPs with different concentrations was initially calculated after different durations of co-incubation to evaluate their biocompatibility. It was shown that the cell viability

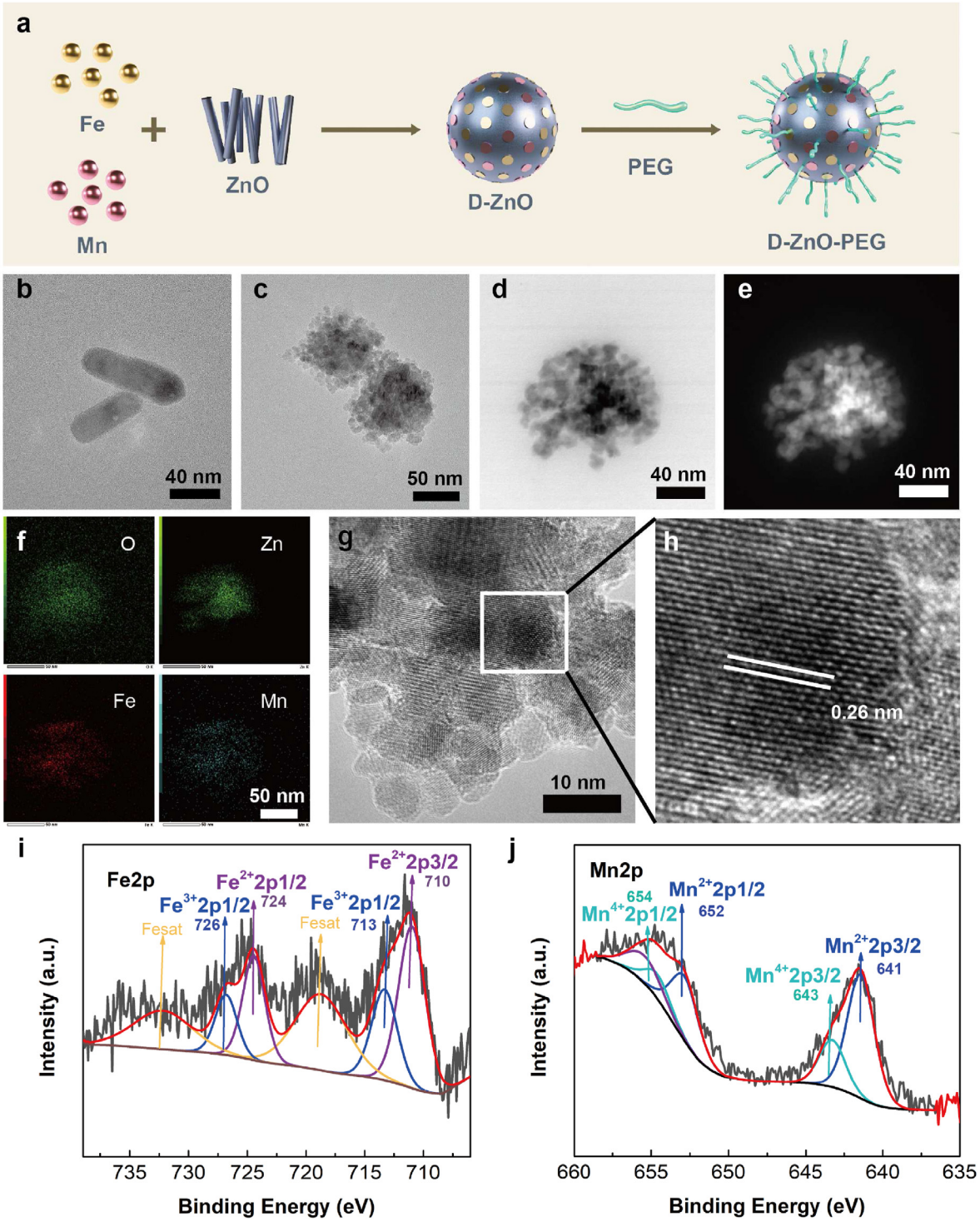

Fig. 2. Synthesis and characterization of D-ZnO-PEG NPs. (a) Schematic illustration of fabrication procedure of D-ZnO-PEG NPs. (b) TEM image of pure ZnO NRs. (c) TEM image of D-ZnO NPs. (d) HAADF-STEM image of D-ZnO NPs, bright field. (e) HAADF-STEM image of D-ZnO NPs, dark field. (f) Elemental mapping of O, Zn, Fe and Mn in D-ZnO NPs. (g, h) HRTEM image of D-ZnO NPs. (i) Fe 2p XPS spectrum of D-ZnO NPs. (j) Mn 2p XPS spectrum of D-ZnO NPs.

behaved no significant decrease even at the highest concentration (200 ppm) for 48 h, proving the relative biosafety in nomal tissues (90.5% of viability at 200 ppm for 48 h) (Fig. 4a). When 0.1 mM H_2O_2 was added to simulate tumor microenvironment and US was applied, cell viability at different concentrations was differently decreased. With the increase of D-ZnO-PEG concentration and the elevation of US energy, the cell viability stepped down to 20% at 200 ppm of concentration and 1.5 W/cm^2 of power density (Fig. 4b). In addition, we compared the therapuetic efficiency of D-ZnO-PEG + US group with other different groups (Control, D-ZnO-PEG, US, ZnO-PEG + US). Each group was added with 0.1 mM H_2O_2, the concentrations of D-ZnO-PEG and ZnO-PEG were set to be 200 ppm based on Zn content and the US energy was set to be 1.5 W/cm^2. The results showed that the ZnO-PEG + US group exhibited non-negligible decrease of cell viability (69.4%). Notebly, the cell viability of

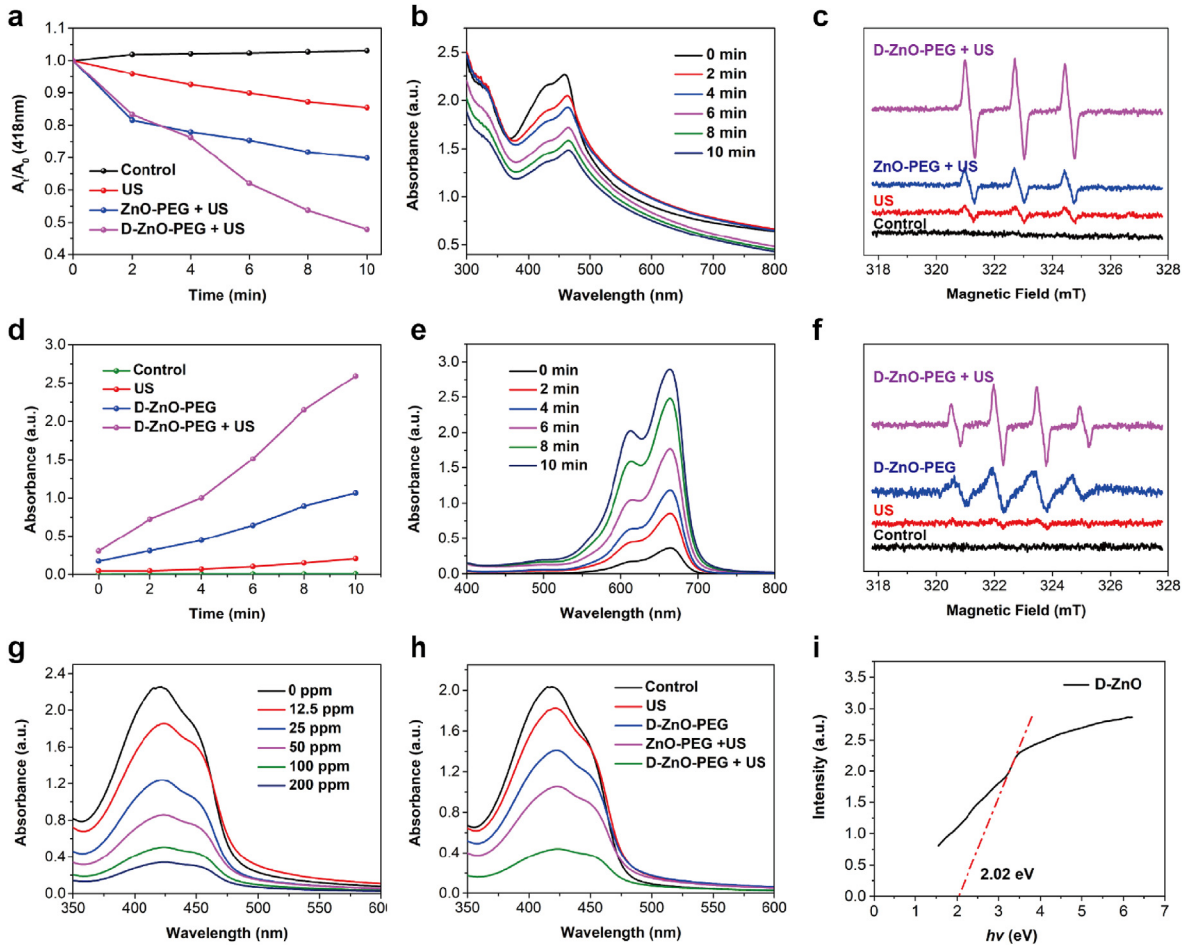

Fig. 3. *In vitro* ferroptosis-augmented SDT effect. (a) Time-dependent DPBF oxidation characteristic peaks of Control, US, ZnO-PEG + US and D-ZnO-PEG + US groups. (b) Time-dependent DPBF oxidation of D-ZnO-PEG + US group. (c) ESR spectra of $^1O_2$ in Control, US, ZnO-PEG + US and D-ZnO-PEG + US groups. (d) Time-dependent TMB oxidation characteristic peaks of Control, US, D-ZnO-PEG and D-ZnO-PEG + US groups. (e) Time-dependent TMB oxidation of D-ZnO-PEG + US group. (f) ESR spectra of •OH in Control, US, D-ZnO-PEG and D-ZnO-PEG + US groups. (g) Zn concentration-dependent GSH depletion of D-ZnO-PEG. (h) GSH depletion comparison of Control, US, D-ZnO-PEG, ZnO-PEG + US and D-ZnO-PEG + US groups. (i) Solid UV–vis spectrum of D-ZnO NPs. The parameters of US irradiation were 1 MHz, 50% duty cycle, 1 W/cm^2.

D-ZnO-PEG + US group significantly dropped to 20%, suggesting the ferroptosis-augmented SDT effect by the doping nanostructure and composition of D-ZnO-PEG nanosonosensitizers (Fig. 4c).

To obtain more accurate anti-tumor efficiency of D-ZnO-PEG NPs, the results carried out by CCK-8 were also evaluated by CLSM and flow cytometry. For CLSM, the 4T1 cancer cells were first co-stained with propidium iodide (PI, dead cells) and calcein AM (AM, live cells), then images of different groups (Control, D-ZnO-PEG, US, ZnO-PEG + US and D-ZnO-PEG + US, each group with 0.1 mM H_2O_2) were observed and the intensities of red fluorescence and green fluorescence were recorded. The D-ZnO-PEG + US group exihited the highest intensity of red fluorescence, which was much higher than ZnO-PEG + US and D-ZnO-PEG group (Fig. 4d). Then, the flow cytometry quantitively determined the apoptosis rates of the above different groups. The apoptosis rate of the D-ZnO-PEG + US group reached 28.8% (early apoptosis) + 23.5% (late apoptosis), which further confirmed the distinct *in vitro* anti-tumor outcome of the enhanced SDT effect by D-ZnO-PEG NPs under US irradiation in TME (Fig. 4e).

To offer accurate mechanism of *in vitro* anti-tumor efficiency, we further employed CLSM and flow cytometry to evaluate the ROS production during the SDT procedure. For the CLSM observation, 2,7-dichlorofluorescein diacetate (DCFH-DA) was used as the probe to detect ROS and DAPI was used as the probe to detect nucleus after different groups of treatment (Control, US, D-ZnO-PEG, ZnO-PEG + US and D-ZnO-PEG + US, each group was added with 0.1 mM H_2O_2). Among all groups, the D-ZnO-PEG and the ZnO-PEG + US group displayed nonnegligible intensity of green fluorescence, confirming the Fenton reaction effect and SDT effect. Most importantly, the D-ZnO-PEG + US group induced the highest intensity of green fluorescence, which indicated the synergistic effect of TME-triggered Fenton reaction and US-triggered SDT enabled by these D-ZnO-PEG nanosonosensitizers (Fig. 5a). Flow cytometry was also used to quantitively evaluate the ROS production among the above all groups. The ROS staining rates were determined to be 46.1% in D-ZnO-PEG, 56.8% in ZnO-PEG + US and 71.5% in D-ZnO-PEG + US, correspondingly (Fig. 5b).

In the ferroptosis program, ROS produced by Fenton reaction damaged the cell membrane and mitochondria, and Fe^{3+} prevented GSH from protecting cell membrane and mitochondria [41,47,48]. Herein, the Fe^{2+} and Mn^{2+} in the doping nanostructure triggered Fenton reaction in the presence of H_2O_2, then the produced Fe^{3+} and Mn^{4+} enhanced GSH consumption effect. Therefore, we observed cell membrane and mitochondria damage by bio-TEM and GSH consumption by western blot analysis. The bio-TEM images showed that the membranes of 4T1 cancer cells were cracked obviously, and the mitochondria were also damaged to varying degrees (Fig. 5c). The key protein expression of ferroptosis glutathione peroxidase 4 (GPX4) was analyzed by western blot to evaluate the GSH consumption in different groups (Control, US, D-ZnO-PEG, ZnO-PEG + US, D-ZnO-PEG + US) [49,50]. The results showed that GPX4

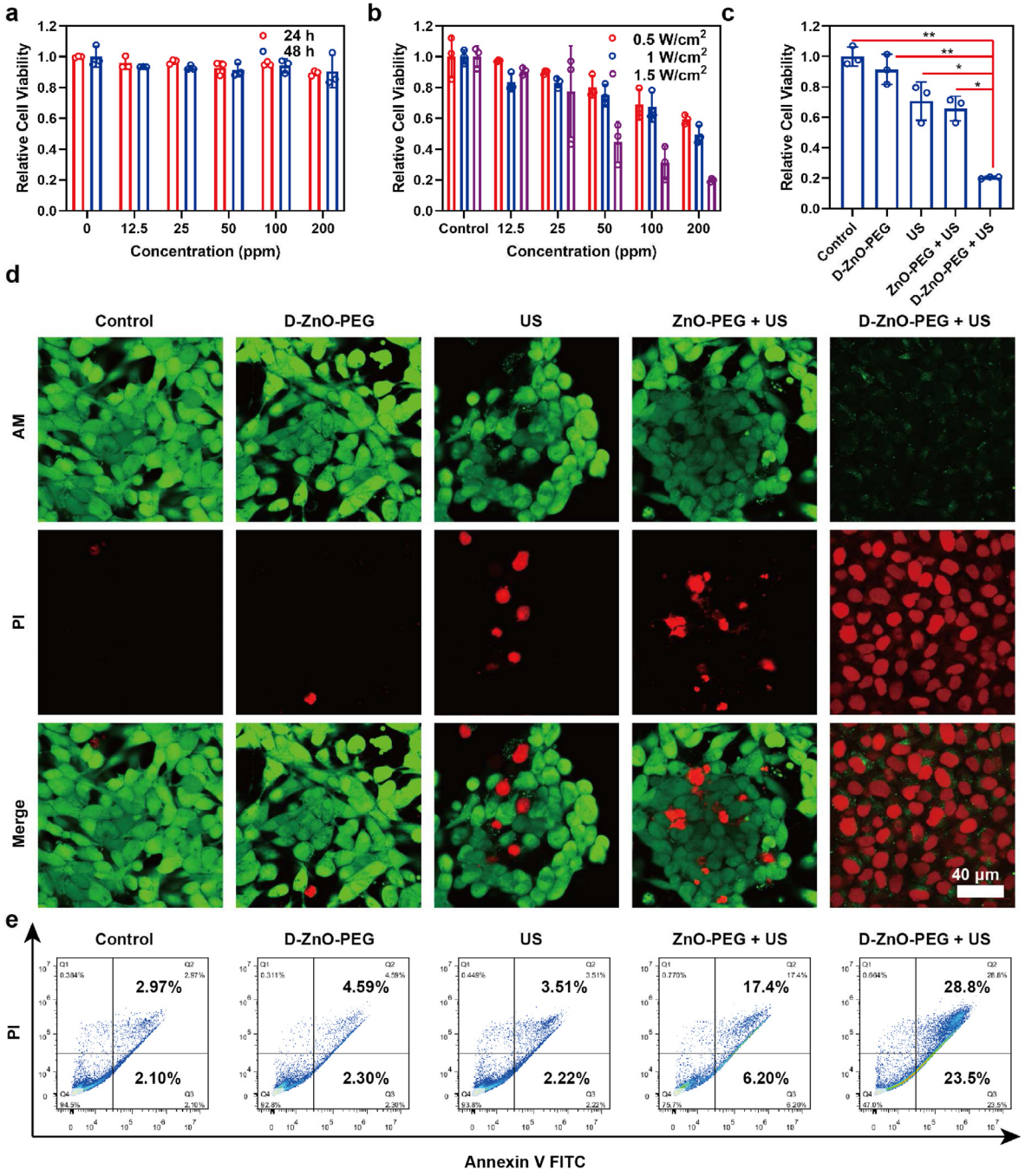

Fig. 4. Intracellular ferroptosis-augmented SDT anti-tumor efficiency, cell viability analysis, live/dead observation by CLSM and flow cytometry. (a) Cytotoxicity anylysis of 4T1 cells after incubation with D-ZnO-PEG for 24 h and 48 h. (b) Relative cell viability dependent on Zn concentration and US power density. (c) Relative cell viability in different groups of treatment (Control, D-ZnO-PEG, US, ZnO-PEG + US and D-ZnO-PEG + US). (d) Confocal images of differently treated 4T1 cancer cells stained with AM and PI. (e) Flow cytometry analysis of differently treated 4T1 cancer cells. The parameters of US energy were 1 MHz, 50% duty cycle, 1.5 W/cm^2.

expression level of D-ZnO-PEG + US group decreased to 0.32 (GPX4/GAPDH) compared with the Control group (1.30). In contrast, the expression of acyl-CoA synthetase long-chain family member 4 (ACSL4), which is a biomarker and contributor of ferroptosis increased to 0.52 (ACSL4/GAPDH) in D-ZnO-PEG + US group compared with the Control group (0.28), confirming the ferroptosis-induced cell membrane damage (Fig. 5d).

Therefore, the underlying mechanism of ferroptosis-augmented SDT against tumor was described as follows. On one hand, the doping of Fe/Mn in the ZnO nanosonosensitizer could augment the ROS production by US-triggered SDT. On the other hand, the Fenton reaction and GSH depletion in ferroptosis process could enhance the tumor cell-killing effect. The synergistic effect by both enhanced SDT and ferroptosis induced by D-ZnO-PEG NPs guarantees the high antitumor efficiency.

2.4. Biological mechanism of ferroptosis-augmented SDT by RNA sequencing

To further determine the biological mechanism of ferroptosis-augmented SDT by D-ZnO-PEG nanosonosensitizers, we employed RNA expression sequencing (RNAseq) for mechanism analysis. Briefly, gene expression profiles of different groups (Control and D-ZnO-PEG + US)

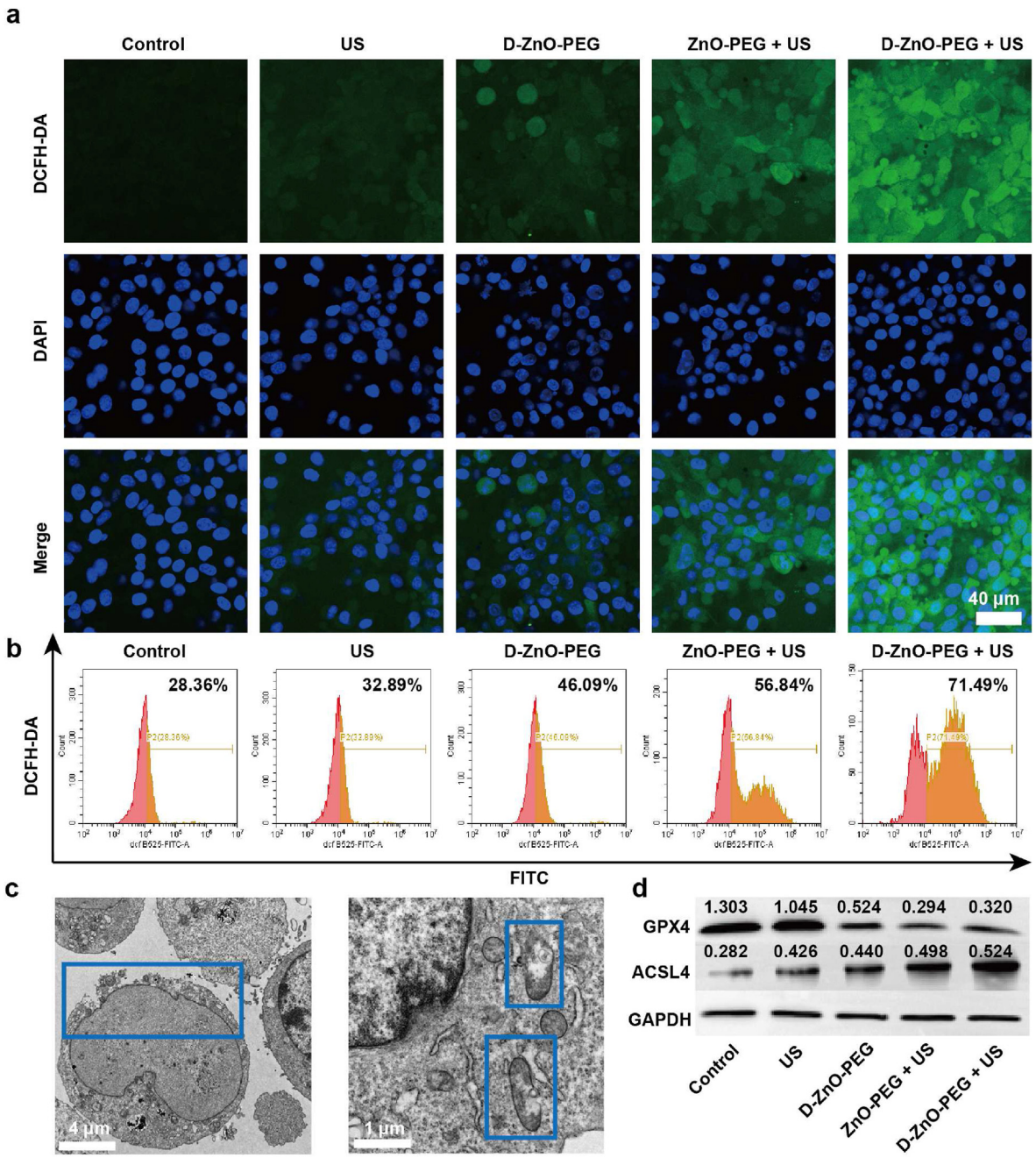

Fig. 5. Intracellular anti-tumor mechanism, ROS detection, bio-TEM and western blot analysis. (a) Confocal images of 4T1 cells in different treatments (Control, US, D-ZnO-PEG, ZnO-PEG + US and D-ZnO-PEG + US) after staining with DCFH-DA and DAPI. (b) Flow cytometry analysis of ROS production in the above groups. (c) Observation of cell membrane and mitochondra damage by bio-TEM. (d) Western blot of GPX4 and ACSL4 in the above groups. The parameters of US irradiation were set as 1 MHz, 50% duty cycle, 1.5 W/cm^2, 2 min.

were analyzed by htseq-count and cufflinks after 4T1 cancer cells were treated [51,52]. The heat map demonstrated 15,776 co-expressed genes between the D-ZnO-PEG + US group and the Control group (Fig. 6a). There were 1998 significantly differentially expressed genes involved in the D-ZnO-PEG + US group according to the volcano map, including 781 up-regulated and 1127 down-regulated mRNAs (Fig. 6b and c). Moreover, the interaction relationship between key genes was illustrated by the protein-protein interactions network analysis (Fig. 6d). For further investigation of the biological functions, the Kyoto Encyclopedia of Genes and Genomes (KEGG) enrichment analysis was performed, in which ferroptosis, apoptosis, the TNF signaling pathway, the MARK signaling pathway and the IL-17 signaling pathway were highly relative to the ferroptosis-augmented SDT effect. Notably, the MARK signaling pathway was related to ROS-induced cell apoptosis, which stressed the effect of US-triggered SDT (Fig. 6e and f) [53].

2.5. *In vivo ferroptosis-augmented SDT against tumor*

The *in vivo* ferroptosis-augmented SDT was further assessed on the mouse model bearing 4T1 tumor cells based on the demonstrated *in vitro* therapeutic performance. It is important to ensure efficient accumulation of D-ZnO-PEG NPs in tumor site for guaranteeing high therapeutic effect. Therefore, we employed *in vivo* fluorescence imaging to monitor the enrichment of D-ZnO-PEG NPs in tumor site directly after intravenous injection of indocyanine green (ICG)-labelled D-ZnO-PEG NPs. With prolonged time, the fluorescence signals in tumor site gradually

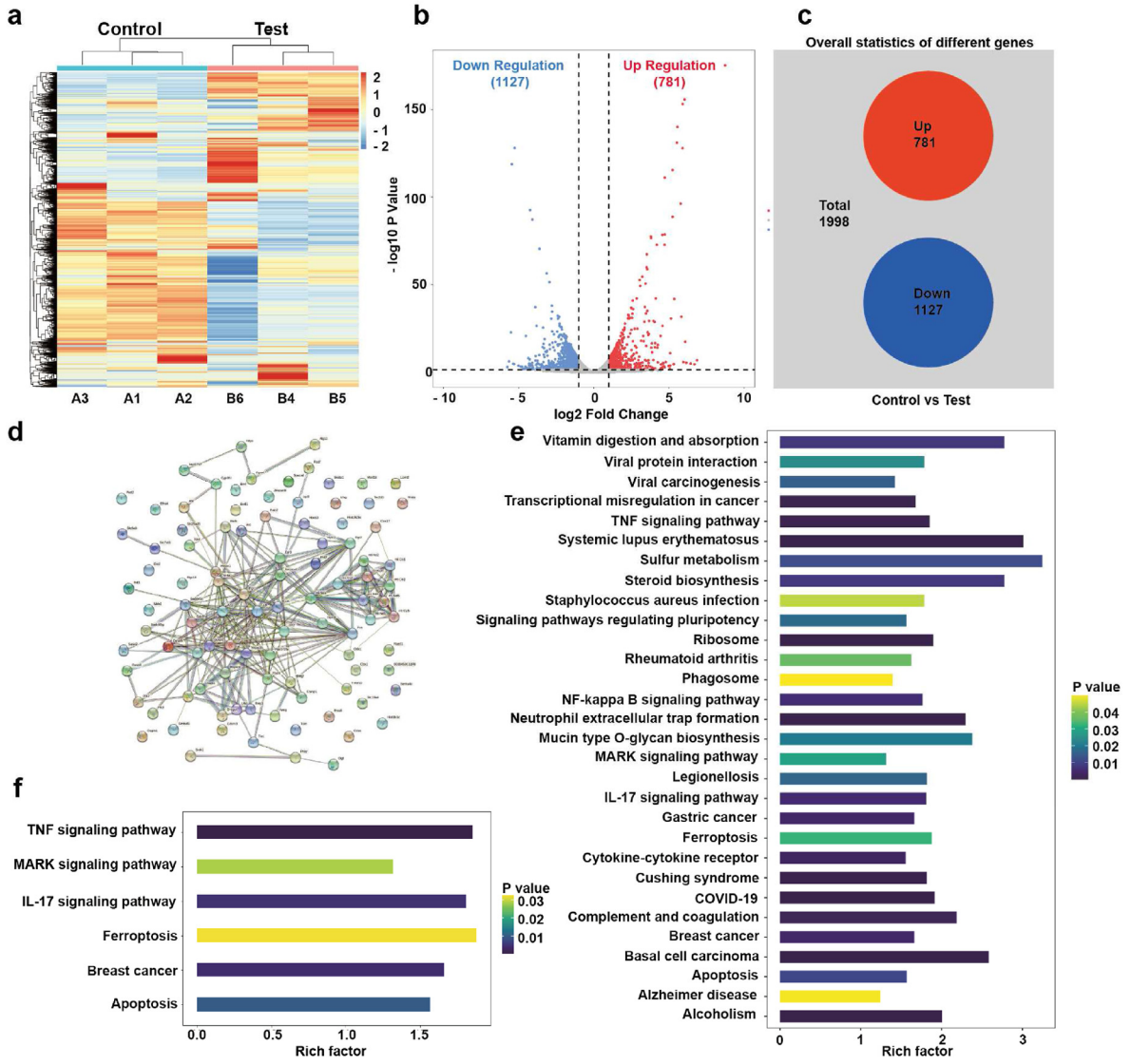

Fig. 6. Biological therapeutic mechanisms of the ferroptosis-augmented SDT by RNA sequencing. (a) The heat map demonstrating co-expressed genes between the D-ZnO-PEG + US group and the Control group. (b) The volcano map demonstrating the upregulated and downregulated genes by ferroptosis-augmented SDT. (c) Overall statistics of 1998 differently expressed genes including 781 up-regulations and 1127 down-regulations. (d) Protein to protein interaction network of genes involved in the major signaling pathway. Histogram of different genes that all enriched in Kyoto Encyclopedia of Genes and Genomes (KEGG) pathway. (f) Histogram of main genes that are mainly related to ferroptosis and apoptosis in Kyoto Encyclopedia of Genes and Genomes (KEGG) pathway.

enhanced to 6 h and faded afterwards until 24 h, indicating the enhanced permeability and retention (EPR) effect for accumulating D-ZnO-PEG NPs into the tumor site (Figs. S8 and S9). To evaluate the *in vivo* biocompatibility and biosafety of D-ZnO-PEG NPs, we performed a series of experiments on healthy Kunming mice after intravenous administration, including body weight monitoring, haematology routine, biochemistry routine and haematoxylin and eosin (H&E) staining. Briefly, the Kunming mice were divided randomly into four groups (Control, ZnO-PEG 20 mg/kg, D-ZnO-PEG 10 mg/kg, D-ZnO-PEG 20 mg/kg), then body weight was recorded every 2 days till the 28th day. All groups of injected mice showed no significant difference in biosafety evaluation indexes compared with the control group (Fig. S10). The haematology and biochemistry indexes in each group were all within normal range after feeding for 4 weeks (Figs. S11 and S12). Moreover, the H&E staining of main organs obtained on the 28th day exhibited no obvious differences among the 4 groups, which further confirmed the desirable biocompatibility and biosafety of D-ZnO-PEG NPs *in vivo* (Fig. S13).

Encouraged by the efficient accumulation and desirable biocompatibility of D-ZnO-PEG NPs, we further conducted *in vivo* antitumor evaluations on nude female 4T1 tumor-bearing balb/c mice, which were divided randomly into 5 groups (Control, US, D-ZnO-PEG, ZnO-PEG + US and D-ZnO-PEG + US, n = 5 in each group). US irradiation was applied at tumor site every other day for 3 times after 6 h post intravenous administration of D-ZnO-PEG NPs (Fig. 7a). Tumor size and body weight of each mouse were measured every 2 days till the last day of 14 days' feeding. Notably, the D-ZnO-PEG and ZnO-PEG + US group showed some sort of tumor suppression (48.7% and 46.8% correspondingly), indicating the effect of both ferroptosis and SDT. Meanwhile, the D-ZnO-PEG + US group induced the most significant degree of tumor suppression (92.8%), confirming the effect of ferroptosis-augmented SDT, which corresponded to the tumor photograph observed on the 14th day after mice sacrifice (Fig. 7b, c, d, e). The H&E staining of main organs and body weight monitoring exhibited no significant differences among all 5 groups during the 14 days' procedure, which further confirmed the high therapeutic biosafety of the as-fabricated D-ZnO-PEG NPs (Figs. S14 and S15).

The therapeutic effect of D-ZnO-PEG NPs was further evaluated by

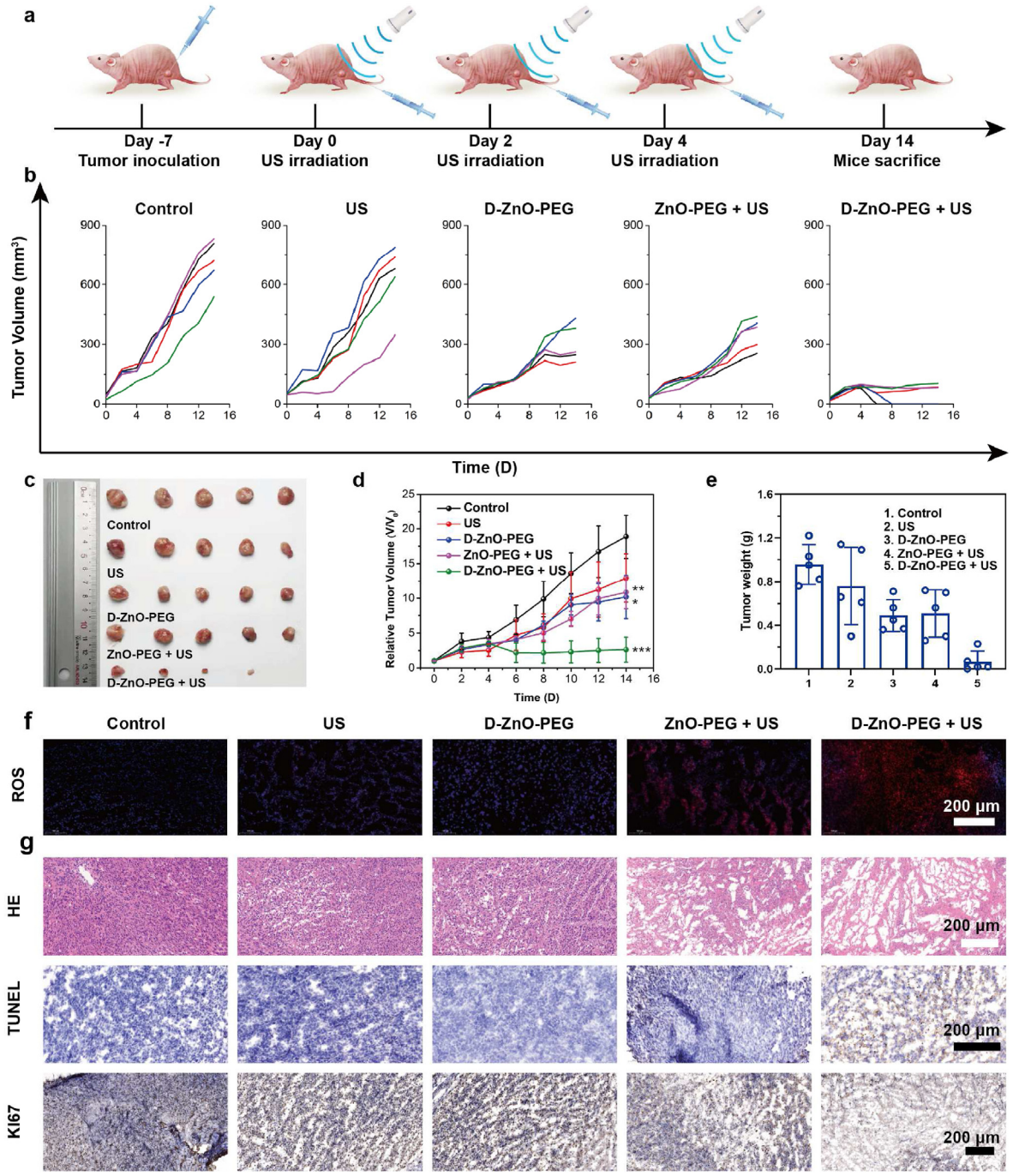

Fig. 7. ***In vivo*** **anti-tumor analysis.** (a) *In vivo* anti-tumor protocol of ferroptosis-augmented SDT on 4T1 tumor-bearing model. (b) Tumor volume of every mouse in different treatment groups (Control, US, D-ZnO-PEG, ZnO-PEG + US and D-ZnO-PEG + US, n = 5 in each group). (c) Picture of tumor from each mouse after sacrifice. (d) Tumor-growth curves of mice dependent on time in 5 groups after different treatments. (n = 5 in each group, *$p < 0.05$, **$p < 0.01$, ***$p < 0.001$). (e) Weight of tumor from each mouse after sacrifice. (f) DCFH-DA staining of different treatment groups to detect ROS production. (g) H&E, TUNEL and Ki67 staining in tumor tissues after different treatments. The applied US irradiation parameters were set to be 1 MHz, 50% duty cycle, 1.5 W/cm^2, 2 min.

DCFH-DA staining, H&E, TUNEL and Ki67 staining to analyze the underlying mechanism of *in vivo* ferroptosis-augmented SDT. For the DCFH-DA staining, the D-ZnO-PEG + US group presented the highest intensity of green fluorescein compared with the other 4 groups, indicating the highest level of ROS production (Fig. 7f). The H&E and TUNEL staining was further employed to evaluate the necrosis and apoptosis of the tumor tissues, where the D-ZnO-PEG + US group (ferroptosis-augmented SDT group) displayed the most degree of necrosis and apoptosis compared to Control, US, D-ZnO-PEG, ZnO-PEG + US groups. Furthermore, the D-ZnO-PEG + US group exhibited the lowest level of Ki67 protein, which is a tumor proliferation marker highly related to cell mitosis, confirming the efficient ferroptosis-augmented SDT induced by such a doping nanostructure under US irradiation (Fig. 7g).

3. Conclusions

In summary, we successfully designed and engineered a distinct Fe/Mn-doped ZnO nanosonosensitizer for simultaneously triggering multiple ferroptosis effect in the specific tumor microenvironment and augmenting the therapeutic efficacy of SDT against tumor. The engineered

D-ZnO-PEG NPs not only tringgered the catalytic Fenton reaction for efficient ROS production and depleted GSH in the presence of Fe and Mn for inducing multiple ferroptosis effect, but also augmented the SDT effect by decreasing the recombination of e^-/h^+ pairs under US irradiation during the SDT procedure. The simultaneously endowed multiple ferroptosis and synergistically enhanced SDT achieved high *in vivo* tumor-suppression efficiency as demonstrated on tumor-bearing mice model. The underlying high therapeutic mechanism was revealed by multiple characterization techniques including the specific RNA sequencing. This work provides the unique paradigm of enhancing the SDT performance of nanosonosensitizers by trasitional metal doping, which is highly informative to further explore other ferroptosis and SDT-based therapeutic modality for efficient tumor nanotherapy with simultaneous desirable therapeutic biosafety, precision, efficency and outcome.

Credit author statement

Y. Chen designed the project. Z. Hu, Y. Zhou, L. Yu, L. Zhang, X. Song, L. Ding, C. Yu carried out the experiments and the characterization. Y. Zhou, Z. Hu, L. Zhang, L. Yu and Y. Chen wrote and revised the paper. All authors participated in the discussions of the results.

Declaration of competing interest

The authors declare that they have no known competing financial interests or personal relationships that could have appeared to influence the work reported in this paper.

Data availability

Data will be made available on request.

Acknowledgments

This article was supported by National Nature Science Foundation of China (Grant No. 81971628), National Natural Science Foundation of China (Grant No. 81901809), Natural Science Foundation of Jiangsu Province (Grant No. BK20200395, BK20190355), National Science Foundation for Young Scientists of China (Grant No. 82102085), Shanghai Science and Technology Program (Grant No. 21010500100) and Basic Research Program of Shanghai Municipal Government (Grant No. 21JC1406002).

Appendix A. Supplementary data

Supplementary data to this article can be found online at https://doi.org/10.1016/j.mtbio.2022.100452.

References

[1] K.D. Kelley, P. Aronowitz, Cancer, Med. Clin. 106 (3) (2022) 411–422.
[2] L.Q. Zhou, P. Li, X.W. Cui, C.F. Dietrich, Ultrasound nanotheranostics in fighting cancer: advances and prospects, Cancer Lett. 470 (2020) 204–219.
[3] H. Hu, W. Feng, X. Qian, L. Yu, Y. Chen, Y. Li, Emerging nanomedicine-enabled/enhanced nanodynamic therapies beyond traditional photodynamics, Adv. Mater. 33 (12) (2021), e2005062.
[4] X. Li, J.F. Lovell, J. Yoon, X. Chen, Clinical development and potential of photothermal and photodynamic therapies for cancer, Nat. Rev. Clin. Oncol. 17 (2020) 657–674.
[5] S. Liang, X. Deng, P. Ma, Z. Cheng, J. Lin, Recent advances in nanomaterial-assisted combinational sonodynamic cancer therapy, Adv. Mater. 32 (47) (2020), e2003214.
[6] C. Zhang, Z. Zeng, D. Cui, S. He, Y. Jiang, J. Li, J. Huang, K. Pu, Semiconducting polymer nano-PROTACs for activatable photo-immunometabolic cancer therapy, Nat. Commun. 12 (1) (2021) 2934.
[7] N. Shah, J. Squire, M. Guirguis, D. Saha, K. Hoyt, K.K. Wang, V. Agarwal, G. Obaid, Deep-tissue activation of photonanomedicines: an update and clinical perspectives, Cancers 14 (8) (2022).
[8] H. Wu, X. Gao, Y. Luo, J. Yu, G. Long, Z. Jiang, J. Zhou, Targeted delivery of chemo-sonodynamic therapy via brain targeting, glutathione-consumable polymeric nanoparticles for effective brain cancer treatment, Adv. Sci. (2022), e2203894.
[9] Y. Hao, C.K. Chung, Z. Gu, T. Schomann, X. Dong, R. Veld, M.G.M. Camps, P. Ten Dijke, F.A. Ossendorp, L.J. Cruz, Combinatorial therapeutic approaches of photodynamic therapy and immune checkpoint blockade for colon cancer treatment, Molecular Biomedicine 3 (1) (2022) 26.
[10] C. Liu, S. Sun, Q. Feng, G. Wu, Y. Wu, N. Kong, Z. Yu, J. Yao, X. Zhang, W. Chen, Z. Tang, Y. Xiao, X. Huang, A. Lv, C. Yao, H. Cheng, A. Wu, T. Xie, W. Tao, Arsenene nanodots with selective killing effects and their low-dose combination with ß-elemene for cancer therapy, Adv. Mater. 33 (37) (2021), 2102054.
[11] C. Feng, J. Ouyang, Z. Tang, N. Kong, Y. Liu, L. Fu, X. Ji, T. Xie, O.C. Farokhzad, W. Tao, Germanene-based theranostic materials for surgical adjuvant treatment: inhibiting tumor recurrence and wound infection, Matter 3 (1) (2020) 127–144.
[12] J. Ouyang, L. Zhang, L. Li, W. Chen, Z. Tang, X. Ji, C. Feng, N. Tao, N. Kong, T. Chen, Y.N. Liu, W. Tao, Cryogenic exfoliation of 2D stanene nanosheets for cancer theranostics, Nano-Micro Lett. 13 (1) (2021) 90.
[13] X. Ji, L. Ge, C. Liu, Z. Tang, Y. Xiao, W. Chen, Z. Lei, W. Gao, S. Blake, D. De, B. Shi, X. Zeng, N. Kong, X. Zhang, W. Tao, Capturing functional two-dimensional nanosheets from sandwich-structure vermiculite for cancer theranostics, Nat. Commun. 12 (1) (2021) 1124.
[14] X. Ji, Y. Kang, J. Ouyang, Y. Chen, D. Artzi, X. Zeng, Y. Xiao, C. Feng, B. Qi, N.Y. Kim, P.E. Saw, N. Kong, O.C. Farokhzad, W. Tao, Synthesis of ultrathin biotite nanosheets as an intelligent theranostic platform for combination cancer therapy, Adv. Sci. 6 (19) (2019), 1901211.
[15] J. Ouyang, Z. Tang, N. Farokhzad, N. Kong, N.Y. Kim, C. Feng, S. Blake, Y. Xiao, C. Liu, T. Xie, W. Tao, Ultrasound mediated therapy: recent progress and challenges in nanoscience, Nano Today 35 (2020), 100949.
[16] C. Wang, Y. Tian, B. Wu, W. Cheng, Recent progress toward imaging application of multifunction sonosensitizers in sonodynamic therapy, Int. J. Nanomed. 17 (2022) 3511–3529.
[17] Z. Guo, Y. Yu, L. Shi, Y. Liao, Z. Wang, X. Liu, X. Lu, J. Wang, Defect engineering triggers exceptional sonodynamic activity of manganese oxide nanoparticles for cancer therapy, ACS Appl. Bio Mater. (2022), 0811.
[18] J. Ouyang, A. Xie, J. Zhou, R. Liu, L. Wang, H. Liu, N. Kong, W. Tao, Minimally invasive nanomedicine: nanotechnology in photo-/ultrasound-/radiation-/magnetism-mediated therapy and imaging, Chem. Soc. Rev. 51 (12) (2022) 4996–5041.
[19] W. Chen, C. Liu, X. Ji, J. Joseph, Z. Tang, J. Ouyang, Y. Xiao, N. Kong, N. Joshi, O.C. Farokhzad, W. Tao, T. Xie, Stanene-based nanosheets for β-elemene delivery and ultrasound-mediated combination cancer therapy, Angew. Chem. Int. Ed. 60 (13) (2021) 7155–7164.
[20] X. Lin, J. Song, X. Chen, H. Yang, Ultrasound-activated sensitizers and applications, Angew. Chem. Int. Ed. 59 (34) (2020) 14212–14233.
[21] S. Son, J.H. Kim, X. Wang, C. Zhang, S.A. Yoon, J. Shin, A. Sharma, M.H. Lee, L. Cheng, J. Wu, J.S. Kim, Multifunctional sonosensitizers in sonodynamic cancer therapy, Chem. Soc. Rev. 49 (11) (2020) 3244–3261.
[22] X.W. Cui, X.X. Han, L.D. Yu, B. Zhang, Y. Chen, Intrinsic chemistry and design principle of ultrasound-responsive nanomedicine, Nano Today 28 (2019).
[23] X.Q. Qian, Y.Y. Zheng, Y. Chen, Micro/nanoparticle-augmented sonodynamic therapy (SDT): breaking the depth shallow of photoactivation, Adv. Mater. 28 (37) (2016) 8097–8129.
[24] J. An, Y. Hu, K. Cheng, C. Li, X. Hou, G. Wang, X. Zhang, B. Liu, Y. Zhao, M. Zhang, ROS-augmented and tumor-microenvironment responsive biodegradable nanoplatform for enhancing chemo-sonodynamic therapy, Biomaterials 234 (2020), 119761.
[25] X. Pan, W. Wang, Z. Huang, S. Liu, J. Guo, F. Zhang, H. Yuan, X. Li, F. Liu, H. Liu, MOF-Derived double-layer hollow nanoparticles with oxygen generation ability for multimodal imaging-guided sonodynamic therapy, Angew. Chem. Int. Ed. 59 (32) (2020).
[26] M. Wysocki, B. Czarczynska-Goslinska, D. Ziental, M. Michalak, E. Güzel, L. Sobotta, Excited State and Reactive Oxygen Species against Cancer and Pathogens: a Review on Sonodynamic and Sono-Photodynamic Therapy, ChemMedChem, 2022, e202200185.
[27] P. Huang, X.Q. Qian, Y. Chen, L.D. Yu, H. Lin, L.Y. Wane, Y.F. Zhu, J.L. Shi, Metalloporphyrin-encapsulated biodegradable nanosystems for highly efficient magnetic resonance imaging-guided sonodynamic cancer therapy, J. Am. Chem. Soc. 139 (3) (2017) 1275–1284.
[28] Y. Cao, T. Wu, W. Dai, H. Dong, X. Zhang, TiO_2 nanosheets with the Au nanocrystal-decorated edge for mitochondria-targeting enhanced sonodynamic therapy, Chem. Mater. 31 (21) (2019) 9105–9114.
[29] S. Bai, N. Yang, X. Wang, F. Gong, Z. Dong, Y. Gong, Z. Liu, L. Cheng, Ultrasmall iron-doped titanium oxide nanodots for enhanced sonodynamic and chemodynamic cancer therapy, ACS Nano 14 (11) (2020) 15119–15130.
[30] S. Liang, X.R. Deng, G.Y. Xu, X. Xiao, M.F. Wang, X.S. Guo, P.A. Ma, Z.Y. Cheng, D. Zhang, J. Lin, A novel Pt-TiO_2 heterostructure with oxygen-deficient layer as bilaterally enhanced sonosensitizer for synergistic chemo-sonodynamic cancer therapy, Adv. Funct. Mater. 30 (13) (2020).
[31] V. Puspasari, A. Ridhova, A. Hermawan, M.I. Amal, M.M. Khan, ZnO-based antimicrobial coatings for biomedical applications, Bioproc. Biosyst. Eng. (2022) 1–25.
[32] H.S. Rahman, H.H. Othman, R. Abdullah, H. Edin, N.A. Al-Haj, Beneficial and toxicological aspects of zinc oxide nanoparticles in animals, J. Vet. Med. Sci. 8 (4) (2022) 1769–1779.
[33] Y. Liu, Y. Wang, W.Y. Zhen, Y.H. Wang, S.T. Zhang, Y. Zhao, S.Y. Song, Z.J. Wu, H.J. Zhang, Defect Modified Zinc Oxide with Augmenting Sonodynamic Reactive Oxygen Species Generation, Biomaterials, 2020, p. 251.

[34] S. Garg, N. Goel, Photodegradation of dye using Polythiophene/ZnO nanocomposite: a computational approach, J. Mol. Graph. Model. 117 (2022), 108285.
[35] I. Djerdj, G. Garnweitner, D. Arcon, M. Pregelj, Z. Jaglicic, M. Niederberger, Diluted magnetic semiconductors: Mn/Co-doped ZnO nanorods as case study, J. Mater. Chem. 18 (43) (2008) 5208–5217.
[36] Y. Chen, K. Cui, T. Liu, M. Cui, Y. Ding, Y. Chen, X. Chen, W.W. Li, C.X. Li, Enhanced Degradation of Sulfamethoxazole by Non-radical-dominated Peroxymonosulfate Activation with Co/Zn Co-doped Carbonaceous Catalyst: Synergy between Co and Zn, Science of the Total Environment, 2022, 158055.
[37] R. Rohani, N.S.F. Dzulkharnien, N.H. Harun, I.A. Ilias, Green approaches, potentials, and applications of zinc oxide nanoparticles in surface coatings and films, Bioinorgan. Chem. Appl. 2022 (2022), 3077747.
[38] B.B. Ding, P. Zheng, P.A. Ma, J. Lin, Manganese oxide nanomaterials: synthesis, properties, and theranostic applications, Adv. Mater. 32 (10) (2020).
[39] F. Gong, L. Cheng, N. Yang, O. Betzer, L. Feng, Q. Zhou, Y. Li, R. Chen, R. Popovtzer, Z. Liu, Ultrasmall oxygen-deficient bimetallic oxide $MnWO_x$ nanoparticles for depletion of endogenous GSH and enhanced sonodynamic cancer therapy, Adv. Mater. 31 (23) (2019).
[40] J. Wang, W. Kong, H. Jin, C. Li, Q. Luo, Y. Luo, C. Yuan, J. Lu, L. Zhang, X. Liu, Tumor microenvironment responsive theranostic agent for enhanced chemo/chemodynamic/photothermal therapy, Colloids Surf. B Biointerfaces 218 (2022), 112750.
[41] J. Li, X. Tian, J. Liu, Y. Mo, X. Guo, Y. Qiu, Y. Liu, X. Ma, Y. Wang, Y. Xiong, Therapeutic material basis and underling mechanisms of Shaoyao decoction-exerted alleviation effects of colitis based on GPX4-regulated ferroptosis in epithelial cells, Chin. Med. 17 (1) (2022) 96.
[42] X. Han, J. Huang, X. Jing, D. Yang, H. Lin, Z. Wang, P. Li, Y. Chen, Oxygen-deficient black titania for synergistic/enhanced sonodynamic and photoinduced cancer therapy at near infrared-II biowindow, ACS Nano 12 (5) (2018) 4545–4555.
[43] Y. Zhou, L. Yu, C. Dong, J. Liu, B. Yang, Y. Chen, Z. Hu, Two-dimensional semiconductor heterojunction nanostructure for mutually synergistic sonodynamic and chemoreactive cancer nanotherapy, Chem. Eng. J. 431 (2022), 134017.
[44] Z.Y. Shen, J.B. Song, B.C. Yung, Z.J. Zhou, A.G. Wu, X.Y. Chen, Emerging strategies of cancer therapy based on ferroptosis, Adv. Mater. 30 (12) (2018).
[45] N. Wiesmann, W. Tremel, J. Brieger, Zinc oxide nanoparticles for therapeutic purposes in cancer medicine, J. Mater. Chem. B 8 (23) (2020) 4973–4989.
[46] F. Gong, L. Cheng, N. Yang, Y. Gong, Y. Ni, S. Bai, X. Wang, M. Chen, Q. Chen, Z. Liu, Preparation of $TiH_{(1.924)}$ nanodots by liquid-phase exfoliation for enhanced sonodynamic cancer therapy, Nat. Commun. 11 (1) (2020) 3712.
[47] L. Wang, Y. Chen, J. Zhao, D. Luo, W. Tian, Analysis and prediction model of ferroptosis related genes in breast cancer, Transl. Cancer Res. 11 (7) (2022) 1970–1976.
[48] J. Chen, X. Zhu, D. Chen, L. Jin, W. Xu, W. Yu, L. Zhang, A multiomic ferroptosis-associated prognostic signature incorporating epigenetic and transcriptional biomarkers for hepatocellular carcinoma, Transl. Cancer Res. 11 (7) (2022) 1889–1897.
[49] Z. Li, Z. Zhu, Y. Liu, Y. Liu, H. Zhao, Function and regulation of GPX4 in the development and progression of fibrotic disease, J. Cell. Physiol. 237 (7) (2022) 2808–2824.
[50] C. Cui, F. Yang, Q. Li, Post-translational modification of GPX4 is a promising target for treating ferroptosis-related diseases, Front. Mol. Biosci. 9 (2022), 901565.
[51] X. Yang, D. Cao, W. Ma, S. Gao, G. Wen, J. Zhong, Wnt signaling in triple-negative breast cancers: its roles in molecular subtyping and cancer cell stemness and its crosstalk with non-coding RNAs, Life Sci. 300 (2022), 120565.
[52] Y. Yi, M. Wu, H. Zeng, W. Hu, C. Zhao, M. Xiong, W. Lv, P. Deng, Q. Zhang, Y. Wu, Tumor-derived exosomal non-coding RNAs: the emerging mechanisms and potential clinical applications in breast cancer, Front. Oncol. 11 (2021), 738945.
[53] L. Zhou, C. Dong, L. Ding, W. Feng, L. Yu, X. Cui, Y. Chen, Targeting ferroptosis synergistically sensitizes apoptotic sonodynamic anti-tumor nanotherapy, Nano Today 39 (2021), 101212.